

Dynamics and mechanisms of intracellular calcium waves elicited by tandem bubble-induced jetting flow^a

¹Fenfang Li; ¹Chen Yang; ²Fang Yuan; ¹Defei Liao, ¹Thomas Li, ³Farshid Guilak, and ¹Pei Zhong

¹Department of Mechanical Engineering and Materials Science, Duke University, Durham, NC 27708; ²Huacells Corp, Natick, MA 01760; ³Department of Orthopaedic Surgery, Washington University, St. Louis, MO 63110, and Shriners Hospitals for Children, St. Louis, MO 63110

Abstract

Ultrasound-induced cavitation microbubbles can lead to cell injury or mechanotransduction via calcium signaling processes such as intracellular calcium waves (ICWs). However, the mechanisms by which microbubbles stimulate ICWs remain unknown. Using a microfluidic platform with highly controlled bubble-cell interaction, we have identified two distinct types of ICWs – a fast response correlating with significant membrane poration, and a slow response triggered by calcium influx through stretch-activated ion channels. The fast ICWs, distinguished from those under physiological conditions, are associated with cell injuries. We further elicited ICWs without cell injury by displacing integrin-binding beads on the cell membrane under mild cavitation conditions. This study provides mechanistic insights into ICWs for guiding ultrasound therapy in tissue modification, drug delivery, and cell mechanotransduction.

Keywords: Intracellular calcium wave; cavitation bioeffects; single cell analysis; cell injury; mechanotransduction; microfluidics

Introduction

Cavitation can produce a broad and diverse range of bioeffects during ultrasound therapy. Although cavitation-induced calcium responses have been reported during sonoporation (1, 2), and ultrasonic neuromodulation (3), the mechanism whereby the calcium ion (Ca^{2+}) transient is initiated, its propagation characteristics, and relationship to downstream bioeffects such as cell injury and mechanotransduction have not been carefully examined (4), especially at the single cell level. For example, it is unclear how the Ca^{2+} transients produced during sonoporation, with or without membrane poration, differ from each other quantitatively, and whether different mechanisms are involved (2, 5). In addition, mechanotransduction applications such as sonogenetics have gained increasing attention as a non-invasive method for neuromodulation where microbubbles are required to facilitate the cellular response (3). Despite the growing interest and potential, the role of cavitation-induced Ca^{2+} transients in such mechanotransduction processes is also not well understood. Moreover, minimum injury and membrane poration are desirable in sonogenetics and other ultrasonic mechanotransduction applications. Altogether, a fundamental understanding of the mechanisms underpinning cavitation-induced Ca^{2+} response and associated bioeffects will be critical for exploiting the full potential of ultrasound in targeted molecular delivery, tissue modification, and sonogenetics through mechanosensory responses (3) that can produce the intended therapeutic outcome with minimal adverse effects (4).

Ca^{2+} -mediated signaling can be triggered when extracellular Ca^{2+} influxes into the cell through plasma membrane, or Ca^{2+} is released from intracellular stores, such as the endoplasmic reticulum (ER). This signal transduction is often accompanied by an intracellular Ca^{2+} wave (ICW). Although Ca^{2+} signaling has been well investigated in biology (6, 7) regarding the role of ion channels and intracellular release, limited work has been carried out on the Ca^{2+} response to membrane poration and cell injury, which occurs frequently in ultrasound therapy with exposure to cavitation. In particular, cavitation can generate impulsive shear flows, and high-strain-rate cell membrane deformation that may result in transient membrane poration and sublethal cell injury (8-10). Therefore, it is important to investigate cavitation-induced Ca^{2+} signaling and other cell response subjected to such high-strain rate mechanical loading. However, challenges exist for current techniques of ultrasound-generated cavitation bubbles to dissect the complex bubble(s)-cell interaction due to the randomness in bubble generation and dynamics. Furthermore, bubble-bubble interaction or bubble collapse near a boundary with cells can lead to jet formation (11, 12), which are common in therapeutic ultrasound. In this study, we therefore examined the dynamics and mechanisms of intracellular Ca^{2+} response in single HeLa cells with a microfluidic platform that offers precise control of the dynamic bubble(s)-cell interactions (9, 13), in which cells are stimulated by the directional jetting flow from laser-induced tandem bubbles (TBs) at different standoff distance S_d , corresponding to various degrees of membrane deformation.

Body

^aA full-length version of this work has been submitted to PNAS for consideration of possible publication.

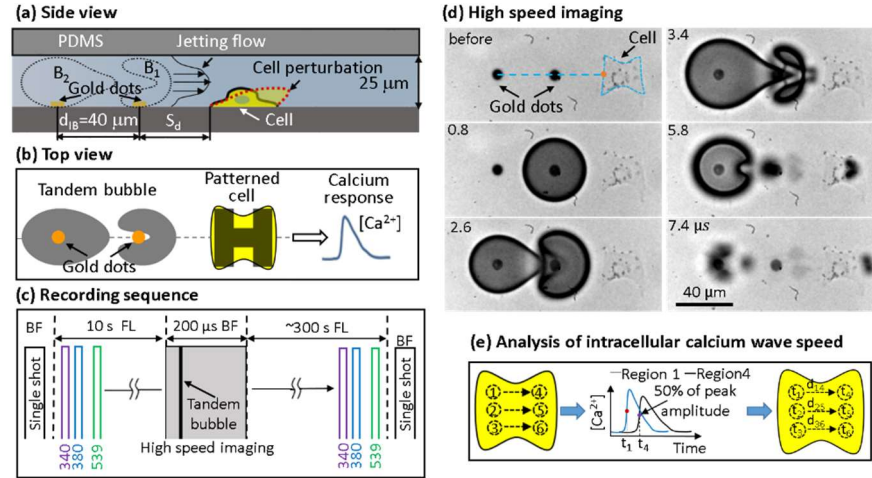


Fig. 1. Schematic diagrams of experimental design and data analysis. (a) Side view and (b) top view of TB interaction with a single cell grown on an H-shaped pattern in a microfluidic channel. (c) Recording sequences for bright field (BF) imaging of cell morphology, simultaneous monitoring of intracellular Ca^{2+} transients (340, 380 nm excitation) and membrane poration (539 nm excitation) through fluorescence (FL) imaging, and high-speed imaging of tandem bubble interaction with jet formation. (d) Example of high-speed image sequence showing the interaction of laser-generated TB from gold dots with a HeLa cell. (e) Protocol used for intracellular Ca^{2+} wave speed (C_{ICW}) analysis.

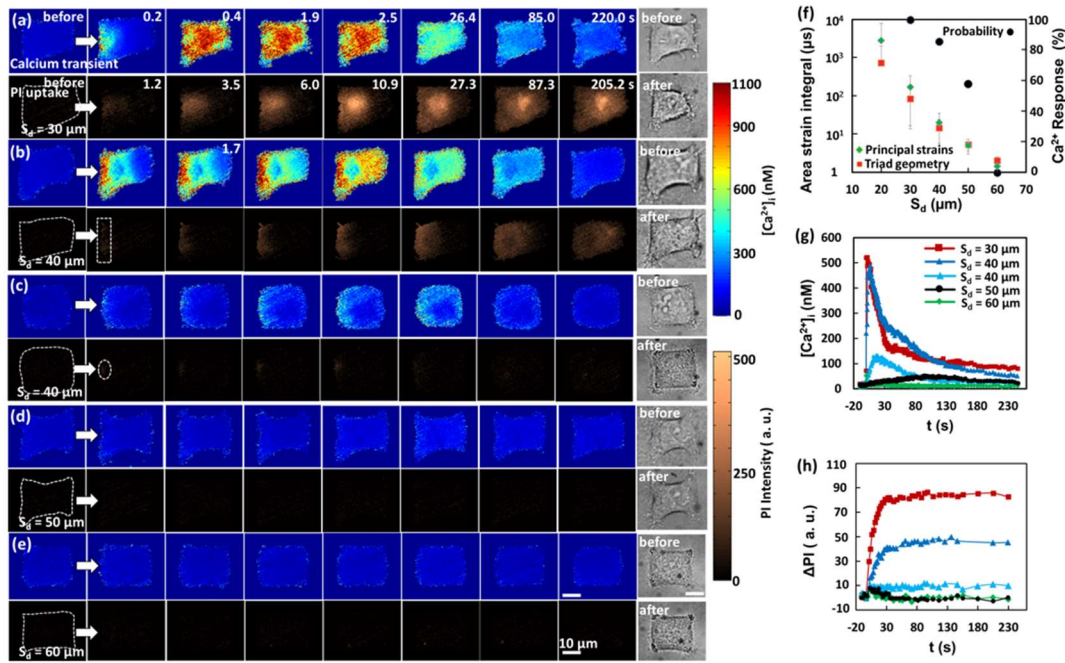


Fig. 2. Typical intracellular Ca^{2+} response and PI uptake induced by TB treatment at various S_d . (a)-(e) Image sequences showing intracellular Ca^{2+} response (top row) and PI uptake (bottom row) in five representative individual cells at $S_d = 30, 40$ (two cells), 50 and 60 μm , respectively. Bright field images of the cell before and after the treatment are shown on the right. The timing for the image sequences shown in (b) - (e) are the same as in (a) except as otherwise marked on the image. The white arrows indicate the jetting flow direction. The cell contour before treatment is outlined with white dashed lines in the first PI image. Cells were exposed to tandem bubbles at $t = 0$. (f) Ca^{2+} response probability (black circles) and area strain integral (shown in green and red symbols) at different S_d ($n = 19, 21, 19, 10$ for the Ca^{2+} response probability at $S_d = 30, 40, 50, 60$ μm , respectively). (g) and (h) are the temporal profiles of averaged intracellular Ca^{2+} concentration and PI uptake inside each individual cell shown in (a)-(e), respectively. The colors and symbols used for different S_d are the same in (g) and (h). All scale bars denote 10 μm .

Directional perturbation of single cells from TB-generated jetting flow. TBs ($R_{\text{max}} = 25 \pm 1$ μm) were produced by focusing two pulsed Nd:YAG laser beams ($\lambda = 532$ nm, 5-ns pulse duration, 2.5 μs interpulse delay) onto a pair of gold dots (15-nm thick and 6 μm in diameter, with an interbubble distance of $d_{\text{IB}} = 40$ μm) patterned on the glass substrate of a microfluidic channel ($H = 25$ μm , Fig. 1a). An individual HeLa cell was captured and grown on a H-shaped island (32 X 32 μm) covered with fibronectin (Fig. 1 (a-b)) nearby ($\gamma = S_d/R_{\text{max}} = 1.2 - 2.4$). Because the two

bubbles are oscillating out of phase, they repel each other by the secondary Bjerknes forces (14), resulting in an outward directional jet formation between 3.0 and 5.0 μs (Fig. 1d), which imposes a highly localized shear stress and stress gradient onto the target cell. Sequential fluorescence (FL) imaging of the intracellular Ca^{2+} transients (340, 380 nm excitation of fura-2) and membrane poration (539 nm excitation of PI) was first recorded at baseline level for 10 s before high-speed imaging of the TB interaction and jet formation, followed by a sequence of FL imaging again in the target cell for 300 s (Fig. 1c). Before and after the TB treatment, changes in cell morphology were also documented by single-shot bright field (BF) images. Cell injury is assessed by PI uptake and BF cell morphology change. To quantify the propagation of intracellular Ca^{2+} transient, the Ca^{2+} response profiles from the cell leading edge (small regions 1, 2, 3) to the trailing edge (small regions 4, 5, 6) are analyzed based on the time-of-flight in 50% rise time of individual pairs (Fig. 1e).

Spatiotemporal evolution of intracellular Ca^{2+} response and PI uptake induced by TB at various S_d . Figure 2 shows the image sequences of the typical intracellular Ca^{2+} response (top row) and PI uptake (bottom row) for individual cells treated with TB at $S_d = 30$ (a), 40 (b-c), 50 (d), 60 (e) μm , respectively. In general, the intensity of the Ca^{2+} response and PI uptake showed a clear S_d dependency, with both signals initiated at the leading edge of the cell facing the jetting flow (indicated by the white arrows) and propagated toward the trailing edge (Fig. 2 (a-c)). The probability of an evoked Ca^{2+} response was found to drop progressively with S_d (circles in Fig. 2f), varying from 100% at $S_d = 30$ μm to no response at $S_d = 60$ μm . This S_d dependency in Ca^{2+} response may be associated with the exponentially decaying shear stress experienced by the target cells at increased S_d (9, 13). The resultant area strain integral (with time) is shown by the diamonds and squares in Fig. 2f, representing their upper- and lower-bound values (9). The average $[\text{Ca}^{2+}]_i$ and PI uptake (ΔPI) within the individual cells shown in Fig. 2 (a-e) are plotted vs. time in Fig. 2g and Fig. 2h, respectively. At $S_d = 30$ μm (or $\gamma = 1.2$), a fast Ca^{2+} response with short rise time ($t_r = 2.2$ s) and large $[\text{Ca}^{2+}]_i$ change (523 nM) was produced, which was accompanied by a high PI uptake (Fig. 2 (a, g, h)). In contrast, at $S_d = 50$ μm (or $\gamma = 2$), a slow Ca^{2+} response with long t_r (99 s) and small $[\text{Ca}^{2+}]_i$ change (38 nM) was observed, associated with negligible PI uptake, see Fig. 2 (d, g and h). At $S_d = 40$ μm , a variety of responses ranging from fast to slow Ca^{2+} transients were obtained, corresponding from high to low PI uptake, see Fig. 2 (b, c, g, h). Finally, at $S_d = 60$ μm , neither Ca^{2+} response nor PI uptake was observed (Fig. 2 (e-h)).

Quantification of calcium response and intracellular calcium wave propagation. Overall, C_{ICW} (mean \pm s.d.) was found to be 57 ± 21 $\mu\text{m/s}$ at $S_d = 30$ μm , which is significantly higher than the corresponding values of 14 ± 15 $\mu\text{m/s}$ at $S_d = 40$ μm and 4 ± 3 $\mu\text{m/s}$ at $S_d = 50$ μm (Fig. 3a). The corresponding probabilities of membrane poration and Ca^{2+} response at different S_d are shown in Fig. 3b. At $S_d = 30$ μm the probability of Ca^{2+} response and membrane poration are both 100%. In contrast, at $S_d = 50$ μm , 44% of the cells showed a Ca^{2+} response with negligible PI uptake. We also examined the correlations between $\Delta[\text{Ca}^{2+}]_{i(\text{max})}$ (in filled symbols) or C_{ICW} (in open symbols) with PI uptake (Fig. 3c). The results showed two types of Ca^{2+} responses that may be delineated by thresholds at PI uptake = 10 (a. u.) and $C_{\text{ICW}} = 30$ $\mu\text{m/s}$, respectively (see the horizontal dashed lines in Fig. 3 (a, c)). In particular, the data points in the $S_d = 50$ μm group (circles) are below these thresholds (i.e., in the lower left quadrant) while most of the data in the $S_d = 30$ μm group (squares) are above these thresholds (i.e., in the upper right quadrant). Furthermore, the value of C_{ICW} was found to scale linearly with $(\Delta[\text{Ca}^{2+}]_{i(\text{max})}/t_r)^{1/2}$ (Fig. 3c inset), which is consistent with previous models of ICW propagation (15, 16).

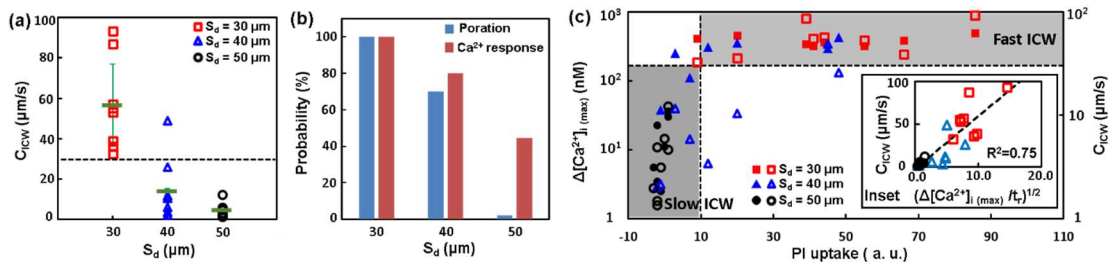


Fig. 3. Quantification of Ca^{2+} response and ICW propagation. (a) C_{ICW} vs. S_d . The error bars indicate the standard deviation. (b) Membrane poration and Ca^{2+} response probability at different S_d . (c) Correlations of the maximum intracellular Ca^{2+} concentration change $\Delta[\text{Ca}^{2+}]_{i(\text{max})}$ (filled symbols) and C_{ICW} (open symbols) vs. PI uptake in the cytosol at $S_d = 30 - 50$ μm . The dashed lines indicate separation of data based on the threshold of PI uptake of 10 (a. u.), and C_{ICW} of 30 $\mu\text{m/s}$. Inset: C_{ICW} vs. the square root of concentration change rate $(\Delta[\text{Ca}^{2+}]_{i(\text{max})}/t_r)^{1/2}$, where t_r is the rise time from baseline to peak concentration. The dashed line represents a linear fitting of the data ($R^2=0.75$).

Mechanistic study of intracellular Ca^{2+} response induced by TB treatment. This series of experiments was carried out at $S_d = 30$ and 50 μm , with three representative (high, medium, low) Ca^{2+} response curves shown in each plot of

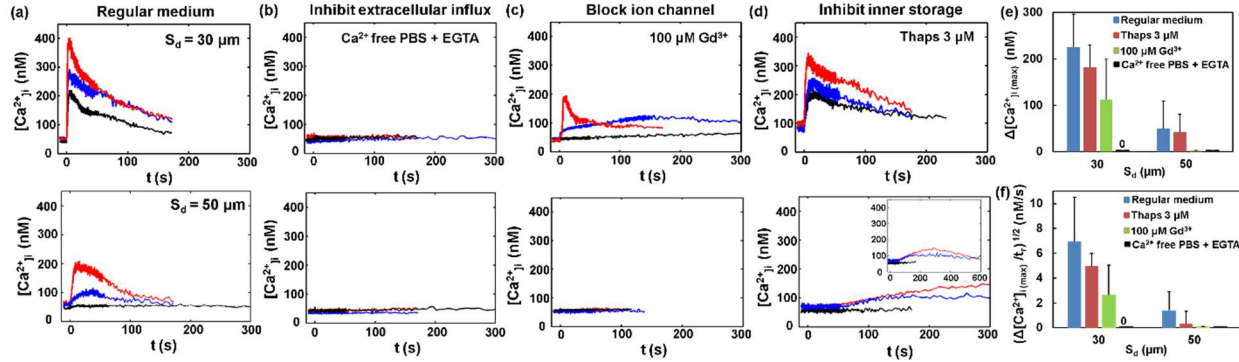


Fig. 4. Mechanistic study of intracellular Ca^{2+} response induced by TB treatment. Ca^{2+} response profiles at $S_d = 30$ and $50 \mu\text{m}$ (a) in regular culture medium; (b) in Ca^{2+} free culture medium (Ca^{2+} free 1x PBS with 0.5 mM EGTA added as Ca^{2+} chelator); (c) in culture medium with $100 \mu\text{M}$ Gd^{3+} to block non-specific mechanosensitive ion channel; (d) in culture medium with $3 \mu\text{M}$ Thaps to inhibit ER Ca^{2+} -ATPases prior to TB treatment and thus affecting Ca^{2+} release. Comparison of Ca^{2+} responses from groups of individual cells treated by TB in regular culture medium (blue), with $3 \mu\text{M}$ Thaps (red), with $100 \mu\text{M}$ Gd^{3+} (green), and in Ca^{2+} free culture medium (black) – (e) $\Delta[\text{Ca}^{2+}]_{i(\text{max})}$ and (f) $(\Delta[\text{Ca}^{2+}]_{i(\text{max})}/t_r)^{1/2}$ vs. $S_d = 30$ and $50 \mu\text{m}$. Data are shown in mean \pm standard deviation ($N = 10, 3, 4, 3$ at $S_d = 30 \mu\text{m}$, and $9, 3, 6, 5$ at $S_d = 50 \mu\text{m}$ for regular culture medium, with $3 \mu\text{M}$ Thaps, with $100 \mu\text{M}$ Gd^{3+} , and in Ca^{2+} free culture medium, respectively.)

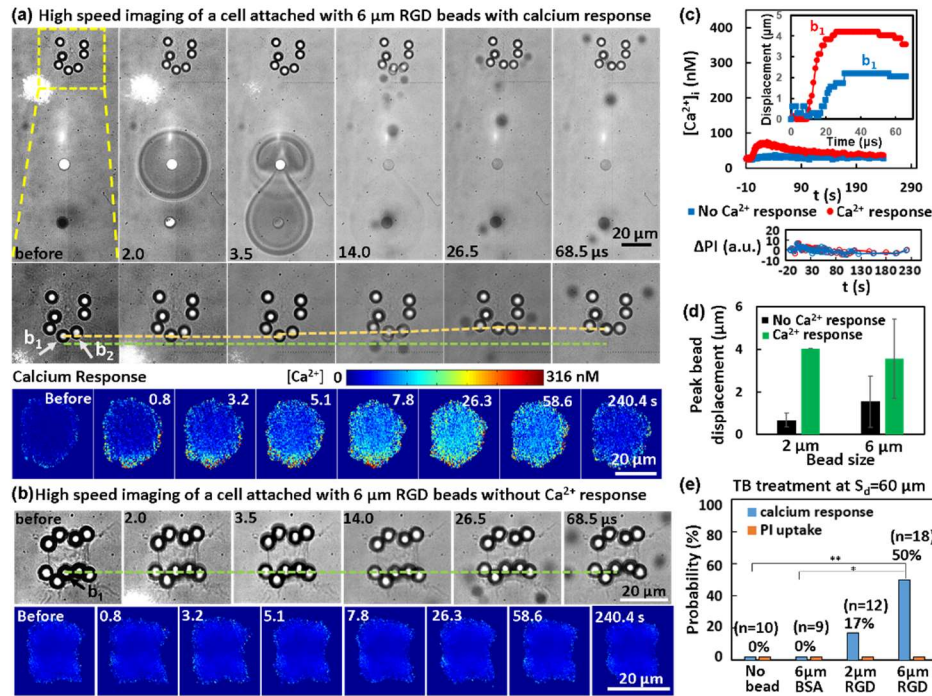


Fig. 5. Beads enhanced Ca^{2+} response at $S_d = 60 \mu\text{m}$. (a) Top row: TB interaction with an H-patterned cell with $6 \mu\text{m}$ RGD beads attached on the cell membrane. Middle row (enlarged region inside the dashed box in top row): the displacement of an individual bead at the cell leading edge (indicated by the yellow dashed line; the green dashed line serves as a reference). Bottom row: fluorescence image sequence showing Ca^{2+} response of the cell in (a). (b) An individual cell attached with $6 \mu\text{m}$ RGD beads were treated with TB, but with no obvious Ca^{2+} response. Top row: the displacement of an individual bead at the cell leading edge (the green dashed line serves as a reference). Bottom row: fluorescence image sequence showing no Ca^{2+} response of the cell (the same colorbar as in (a)). (c) Time evolution of $[\text{Ca}^{2+}]_i$ for the two cells shown in Fig. 5a and Fig. 5b, respectively. Inset shows the time evolution of the displacement of the beads located in the middle of the cell's leading edge (b_1). Bottom row shows there is negligible PI uptake in both cells. (d) Summary of results showing the peak displacement of the bead with the largest displacement (b_1) on the cells for each group (mean \pm s.d.). (e) Probability of Ca^{2+} response and PI uptake in cells with no beads, attached with 2 and $6 \mu\text{m}$ RGD coated integrin-binding beads, or with $6 \mu\text{m}$ BSA-coated non-specific binding beads treated by TB at $S_d = 60 \mu\text{m}$. ** $p < 0.01$, * $p < 0.05$ from Fisher's exact test, the p value between the Ca^{2+} response probability of no beads and $2 \mu\text{m}$ RGD beads is not significant.

Fig. 4(a-d). The control experiment with regular medium is shown in Fig. 4a. The TB-elicited Ca^{2+} response could be completely abolished at both S_d with Ca^{2+} free medium (chelated with EGTA) (Fig. 4b). At $S_d = 50 \mu\text{m}$ where there was no detectable membrane poration, the Ca^{2+} response was completely abolished with $100 \mu\text{M}$ Gd^{3+} blocking mechanosensitive ion channels (Fig. 4c) while at $S_d = 30 \mu\text{m}$ it was found to be either suppressed with reduced

amplitude in $\Delta[\text{Ca}^{2+}]_i$, or very often, converted from fast to slow Ca^{2+} responses. With 3 μM thapsigargin (Thaps) used to inhibit intracellular Ca^{2+} release (Fig. 4d), the Ca^{2+} response was found to be suppressed in both $\Delta[\text{Ca}^{2+}]_{i(\text{max})}$ and $(\Delta[\text{Ca}^{2+}]_{i(\text{max})}/t_r)^{1/2}$ at $S_d = 30 \mu\text{m}$ with a reduced C_{ICW} in the range of 4–11 $\mu\text{m/s}$, compared to the regular medium, see Fig. 4 (d-f). At $S_d = 50 \mu\text{m}$, significantly prolonged Ca^{2+} responses were observed in cells, indicating that the propagation of the Ca^{2+} transient in the cytosol was substantially delayed compared to those in the regular medium. Fig. 4e and Fig. 4f summarize the variations in $\Delta[\text{Ca}^{2+}]_{i(\text{max})}$ and $(\Delta[\text{Ca}^{2+}]_{i(\text{max})}/t_r)^{1/2}$ (proportional to C_{ICW} , see Fig. 3c inset) among the aforementioned culture media. Overall, Thaps, Gd^{3+} , and Ca^{2+} free media were found to affect the amplitude and propagation speed of the Ca^{2+} response. The results indicate that extracellular Ca^{2+} influx is essential for initiating both types of ICWs in the TB-treated HeLa cells: 1) through mechanosensitive ion channels (no injury) in the slow Ca^{2+} response; and 2) through both membrane poration (with injury) and mechanosensitive ion channels during the fast Ca^{2+} response. In both cases, the initiated Ca^{2+} response then propagated through the cytosol most likely via the calcium induced calcium release (CICR) mechanism from the ER (7).

Enhanced intracellular Ca^{2+} response with integrin-binding bead on the cell membrane. At $S_d = 60 \mu\text{m}$, no Ca^{2+} response in a target cell could be induced by the TB because of the diminished strength of the jetting flow (9). We hypothesized that shear flow-cell interaction and resultant membrane deformation may be enhanced by attaching micron-sized beads on the cell surface. Figure 5a shows an example of TB-cell interaction at $S_d = 60 \mu\text{m}$, in which 6 μm RGD (integrin-binding) beads were attached at the cell's leading edge (such as b_1) and found to be significantly displaced from their original locations. Consequently, a mild Ca^{2+} response was elicited inside the cytosol. Fig. 5b shows another individual cell with TB treatment (top row) that showed no Ca^{2+} response (FL images at the bottom row). The maximum bead displacement (e.g., b_1 in Fig. 5b) was found to be significantly less than its counterpart in the responsive cell in Fig. 5a (see Fig. 5c). Moreover, negligible PI uptake was detected in both cases (see ΔPI vs. t profile in Fig. 5c), indicating no cellular injury. For both 2 and 6 μm beads, the maximum bead displacement (of b_1) was found to be significantly larger in Ca^{2+} responsive cells than in non-responsive cells (Fig. 5d). This finding again suggests that large bead displacement or cell membrane stretching is critical for the enhanced Ca^{2+} response at $S_d = 60 \mu\text{m}$. We further observed that the enhancement of Ca^{2+} response was bead-size dependent, increasing from 17% with 2 μm RGD beads to 50% with 6 μm RGD beads (Fig. 5e). No Ca^{2+} response was observed in the control experiment with 6 μm BSA beads that non-specifically bind to the cell membrane ($p < 0.05$ compared to RGD beads).

Discussion and conclusion

The physical characteristics of ICW are highly conserved among various species with C_{ICW} typically in the range of 3 ~ 30 $\mu\text{m/s}$ at 20 °C (16, 17). Quantitatively, C_{ICW} can be scaled by $(J_{\text{eff}} D_{\text{eff}}/C_0)^{1/2}$, where J_{eff} is the effective Ca^{2+} -current density (e.g., 27 $\mu\text{M/s}$), D_{eff} is the effective diffusion constant of Ca^{2+} (e.g., 22 $\mu\text{m}^2/\text{s}$), and C_0 is the $[\text{Ca}^{2+}]_i$ threshold for Ca^{2+} channel activation (e.g., 0.5 μM) (15). Assuming under physiological conditions, D_{eff} and C_0 are constants for each cell type, C_{ICW} is then determined primarily by $(J_{\text{eff}})^{1/2}$. This feature is consistent with our results in Fig. 3c inset, especially for the data in the $S_d = 50 \mu\text{m}$ group and most of the $S_d = 40 \mu\text{m}$ group with C_{ICW} in the range of 3 ~ 30 $\mu\text{m/s}$ (at 20 °C) commonly found among eukaryotic cells (17, 18). In contrast, much higher C_{ICW} (33–93 $\mu\text{m/s}$) was found in the $S_d = 30 \mu\text{m}$ group where all cells showed significant membrane poration and cell injury, which may reduce the $[\text{Ca}^{2+}]_i$ threshold for initiating an ICW (19, 20). Therefore, a high extracellular Ca^{2+} influx (i.e., greater J_{eff}) combined with a low C_0 may contribute to the significantly elevated C_{ICW} observed in the $S_d = 30 \mu\text{m}$ group (Fig. 3a). Furthermore, it is worth noting that the fast ICW induced at $S_d = 30 \mu\text{m}$ may reflect the injury response of the target cell, albeit sublethal, to TB-induced repairable membrane poration, which typically resealed in 30s (see Fig. 2h). The rapid Ca^{2+} influx induced under such conditions may accelerate the depolymerization of cytoskeleton filaments to facilitate internal vesicles (lysosomes) to migrate and patch the rupture site through exocytosis (21, 22), and potentially later on, even the related compensatory response of endocytosis for lesion removal (23). Although the membrane pore is resealed, such a strong Ca^{2+} response is associated with cytotoxicity, manifested by the loss of F-actin stress fibers, cell shrinkage, and even apoptosis observed in this and other studies (24). These collateral injuries, while facilitating the apoptosis of cancer cells in tumor therapy, will limit the range of cavitation-mediated biomedical applications such as gene delivery and neural modulation.

To address this challenge, we have developed a novel strategy to enhance cavitation-induced Ca^{2+} response without injury by attaching micron-sized beads to the cell membrane through the RGD-integrin link (Fig. 5). This enhancement is integrin-binding specific since no Ca^{2+} response was produced with 6 μm BSA beads that were non-specifically attached to cell plasma membrane. The specificity of this response was further confirmed by additional single bubble-cell interaction experiments, which also demonstrated that the enhanced response was significantly suppressed by Gd^{3+} or Ruthenium Red –two well-known inhibitors of mechanosensitive ion channels. Further, we found that the maximum bead displacement in Ca^{2+} responsive cells is significantly larger than that in non-responsive cells attached

with 6 μm integrin-binding beads (Fig. 5). Altogether, our results suggest that the amplified membrane stretch is transmitted through cell surface integrins (25) to activate mechanosensitive ion channels on the cell membrane, and is critical for the enhanced Ca^{2+} response at $S_d = 60 \mu\text{m}$.

In conclusion, we have systematically examined the dynamics and mechanisms of TB-induced ICW at the single cell level. The knowledge acquired in this work shed light on how to target different biological effects such as cell injury and apoptosis, drug delivery and mechanotransduction by tuning the magnitudes of mechanical perturbations through the high strain rate shear flows associated with inertial cavitation and dynamic bubble–bubble interactions that are prevalent in therapeutic ultrasound applications. Here we used cavitation-induced jetting flow to study the ICW in a highly-controlled manner, and the results and insights gained in this work may also apply to single inertial cavitation and other similar mechanical perturbations. Future work may focus on utilizing repeated and programmed cavitation induced shear flow to stimulate cells for long-term bioeffects such as cell proliferation, differentiation and gene expression for tissue growth and wound healing.

References

1. Leow RS, Wan JMF, & Yu ACH (2015) Membrane blebbing as a recovery manoeuvre in site-specific sonoporation mediated by targeted microbubbles. *J. Royal Soc. Interface* 12(105).
2. Fan Z, Kumon RE, Park J, & Deng CX (2010) Intracellular delivery and calcium transients generated in sonoporation facilitated by microbubbles. *J Control Release* 142(1):31-39.
3. Ibsen S, Tong A, Schutt C, Esener S, & Chalasani SH (2015) Sonogenetics is a non-invasive approach to activating neurons in *Caenorhabditis elegans*. *Nature Communications* 6.
4. Hassan MA, Campbell P, & Kondo T (2010) The role of Ca^{2+} in ultrasound-elicited bioeffects: progress, perspectives and prospects. *Drug Discov Today* 15(21-22):892-906.
5. Zhou Y, Shi J, Cui J, & Deng CX (2008) Effects of extracellular calcium on cell membrane resealing in sonoporation. *J Control Release* 126(1):34-43.
6. Berridge MJ (2005) Unlocking the secrets of cell signaling. *Annu Rev Physiol* 67:1-21.
7. Bootman MD & Berridge MJ (1995) The elemental principles of calcium signaling. *Cell* 83(5):675-678.
8. Mohammadzadeh M, Li FF, & Ohl CD (2017) Shearing flow from transient bubble oscillations in narrow gaps. *Phys. Rev. Fluids* 2(1).
9. Yuan F, Yang C, & Zhong P (2015) Cell membrane deformation and bioeffects produced by tandem bubble-induced jetting flow. *Proc Natl Acad Sci U S A* 112(51):E7039-7047.
10. Li FF, Chan CU, & Ohl CD (2013) Yield Strength of Human Erythrocyte Membranes to Impulsive Stretching. *Biophys J* 105(4):872-879.
11. Ohl CD, et al. (2006) Sonoporation from jetting cavitation bubbles. *Biophys J* 91(11):4285-4295.
12. Sankin GN, Yuan F, & Zhong P (2010) Pulsating tandem microbubble for localized and directional single-cell membrane poration. *Phys Rev Lett* 105(7):078101.
13. Fenfang Li FY, Georgy Sankin, Chen Yang, Pei Zhong. (2017) A Microfluidic System with Surface Patterning for Investigating Cavitation Bubble(s)–Cell Interaction and the Resultant Bioeffects at the Single-cell Level. *JoVE* 119.
14. Yuan F, Sankin G, & Zhong P (2011) Dynamics of tandem bubble interaction in a microfluidic channel. *J Acoust Soc Am* 130(5):3339-3346.
15. Kupferman R, Mitra PP, Hohenberg PC, & Wang SSH (1997) Analytical calculation of intracellular calcium wave characteristics. *Biophys J* 72(6):2430-2444.
16. Jaffe LF (1991) The path of calcium in cytosolic calcium oscillations: a unifying hypothesis. *Proc Natl Acad Sci U S A* 88(21):9883-9887.
17. Jaffe LF (1993) Classes and mechanisms of calcium waves. *Cell Calcium* 14(10):736-745.
18. Jaffe LF (2010) Fast calcium waves. *Cell Calcium* 48(2-3):102-113.
19. Carbone E, Marcantoni A, Gancippoli A, Guido D, & Carabelli V (2006) T-type channels-secretion coupling: evidence for a fast low-threshold exocytosis. *Pflugers Arch* 453(3):373-383.
20. Weiss N, et al. (2012) A $\text{Ca}_v3.2$ /syntaxin-1A signaling complex controls T-type channel activity and low-threshold exocytosis. *J Biol Chem* 287(4):2810-2818.
21. McNeil PL & Steinhardt RA (2003) Plasma membrane disruption: repair, prevention, adaptation. *Annu Rev Cell Dev Biol* 19:697-731.
22. Reddy A, Caler E, & Andrews NW (2001) Plasma membrane repair is mediated by Ca^{2+} -regulated exocytosis of lysosomes. *Molecular Biology of the Cell* 12:266a-266a.
23. Idone V, et al. (2008) Repair of injured plasma membrane by rapid Ca^{2+} -dependent endocytosis. *Journal of Cell Biology* 180(5):905-914.
24. Heo J, Sachs F, Wang J, & Hua SZ (2012) Shear-induced volume decrease in MDCK cells. *Cell Physiol Biochem* 30(2):395-406.
25. Matthews BD, Thodeti CK, & Ingber DE (2007) Activation of mechanosensitive ion channels by forces transmitted through integrins and the cytoskeleton. *Mechanosensitive Ion Channels, Part A* 58:59-85.